Analysis of gross vibrational-rotational energy-loss spectra in Li^+-N_2 collisions with the hard-potential model

Masato Nakamura*
College of Science and Technology, Nihon University, Funabashi 274-8501, Japan

Atsushi Ichimura†
Institute of Space and Astronautical Science, JAXA, Sagamihara 229-8510, Japan
(Received 2 November 2004; revised manuscript received 8 March 2005; published 7 June 2005)

The energy-loss spectra in large-angle $Li^+ + N_2$ scatterings are analyzed with the hard-potential model recently proposed, along with the previous hard-shell model. The respective roles of rotational and vibrational excitations are revealed through systematic comparisons of experimental spectra with the models in a wide range of energies (8–100 eV) and angles (40°–120°). The effect of vibrational excitation is found to manifest itself in the shifts of double peaks. Their energy dependence is accounted for by the shape of the equipotential surface as well as by the vibrational suddenness in a collision. The peak position is shown to be sensitive to the curvature of the surface at the orientation angle of 90°, hence to the three-body potential. The unacceptable result of a previous semiclassical calculation is suggested to come from the inappropriate potential taken.

DOI: 10.1103/PhysRevA.71.062701 PACS number(s): 34.50.Ez, 34.10.+x

I. INTRODUCTION

More than two decades ago, Beck and co-workers proposed the *hard-shell model* for rotational excitation in collisions of an atom (or an ion) with a diatomic molecule [1]. The model treats the molecule as a classical rigid rotor with the ellipsoidal surface accounting for the emergence of a rotational rainbow through the instantaneous torque. Because of its simplicity, the model has been widely applied to the energy-loss spectra with individual vibrational-rotational levels left unresolved [2,3]. According to Massey's criterion with the collision time τ_{col}, however, vibrational excitation should be also crucial to the spectra when the collision energy is as high as $10-10^2$ eV.

In a recent paper [4], we have developed a model of an ideally sudden character for rotational *and* vibrational excitations; it is a natural extension of the hard-shell model to a vibrational-rotor molecule. In this *hard-potential model*, the energy-loss spectra are analytically related to a deformable shape of the equipotential surface at the collision energy. It leads to a spectral profile of double peaks (rotational rainbows) for a homonuclear molecule, though their positions are affected by vibrational excitation. It is demonstrated in the classical trajectory (CT) calculation [4] that the spectra are reduced to the hard-potential model when the vibrational period τ_{vib} is artificially taken as $\tau_{vib} \gg \tau_{col}$, while reduced to the hard-shell model when $\tau_{vib} \ll \tau_{col}$. This finding suggests that the combined application of the two models would be useful for analyzing the mechanism of vibrational-rotational excitation through the spectral profiles.

For $Li^+ + N_2$ collisions, the energy-loss spectra have been measured at large scattering angles in a wide range of center-of-mass energies such as $E=4-17$ eV [5,6] and 57–280 eV [7,8]. Several theoretical works have been done for analyzing the spectra, though restricted to the lower energies ($E \leqslant 17$ eV) Among them is the CT calculation [6] with a model potential, indicating that the double-peak structure observed is dominated by rotational excitation. Quantum mechanical calculations have been also carried out with the infinite- order sudden approximation [9], the distorted-wave impulse approximation [10], and the semiclassical time-correlation-function method [11,12]. However, none of them has reproduced the measured spectra satisfactorily; no systematic understanding has been given yet all through the observations.

In the present paper, we make a systematic analysis of gross energy-loss spectra for $Li^+ + N_2$ scatterings in a wide range of energies and angles. Using a realistic potential, we calculate the spectra with the hard-potential model and with the hard-shell model. To make the analyses sounder, we also carry out the CT calculations for a vibrational-rotor molecule and for a rigid-rotor molecule. The results of these calculations are compared with the experiments [6–8] and with the previous semiclassical calculation [12]. It is revealed how the effects of rotational and vibrationl excitations manifest themselves in the spectra and how the spectral profiles vary with the energy, the angle, and the potential.

The methods of calculations are described in the following section. We examine the systematic spectral behaviors in Sec. III and analyze the previous experimental and theoretical results in Sec. IV. Concluding remarks are given in the final section.

II. METHODS OF CALCULATIONS

The interaction potential $V(r,x,R)$ in $Li^+ — N_2$ collisions has been obtained by several *ab initio* calculations [7,13–15,20] as a function of the relative distance r, the orientation angle γ ($x \equiv \cos\gamma$), and the bond length R. How-

*Electronic address: mooming@phys.ge.cst.nihon-u.ac.jp
†Electronic address: ichimura@pub.isas.ac.jp

ever, their results are inappropriate for the present analysis because the x and R dependences are poorly given for the short-range repulsive force. Instead, we construct the potential as a sum of two-body and three-body terms. The two-body Li^+-N potential is taken in the Yukawa form as $V^{(2)}(\rho)=A\exp(-\rho/\lambda)$ with $A=230$ eV and $\lambda=0.32$ Å from the statistical electron model [16]. The three-body correction arises because the electron cloud in the middle of the two N atoms is pushed out when they form an N_2 molecule, hence mimicked by an average of $V^{(2)}$ over the orientations as

$$V^{(3)}(r,R)=\frac{4\delta A\lambda}{rR}\sinh\left(\frac{R}{2\lambda}\right)\exp\left(-\frac{r}{\lambda}\right), \tag{1}$$

where δ is a strength parameter to be adjusted. This form is similar to that proposed by Tanuma *et al.* [17] in the analysis of $Na^+ + N_2$ collisions. The N—N bonding potential is taken in the Morse form as $U(R)=U_0\{\exp[-2(R-R_{eq})/\beta_0]-2\exp[-(R-R_{eq})/\beta_0]\}$ with $U_0=9.8$ eV, $R_{eq}=1.10$ Å, and $\beta_0=0.37$ Å.

In view of the comparison with experiments, we calculate the energy-loss spectrum at a fixed scattering angle θ_{lab} in the laboratory frame and convolute it as

$$\left\langle\frac{d\sigma}{d\epsilon d\Omega_{lab}}\right\rangle_{\Delta\epsilon}=\int_0^1 d\epsilon^*\frac{d\sigma}{d\epsilon^* d\Omega_{lab}}I_{\Delta\epsilon}(\epsilon^*-\epsilon), \tag{2}$$

where the energy transfer ΔE is scaled as $\epsilon=\Delta E/E$. The instrumental function $I_{\Delta\epsilon}(\epsilon^*-\epsilon)$ is taken in the Gaussion form with the full width of half maximum (FWHM) of $\Delta\epsilon$. The width is taken in common among the model and CT calculations for respective spectra so that the comparisons are made on the same ground. The spectra shown below are normalized as $f(\epsilon)=[\langle d\sigma/d\Omega_{lab}d\epsilon\rangle_{\Delta\epsilon}]/[d\sigma/d\Omega_{lab}]$.

In the hard-potential model [4], the specta are determined by the *inelasticity* function $q(x)$ on the equipotential surface at the collision energy E with the equilibrium bond length R_{eq}. The inelasticity is decomposed into the rotational and vibrational contributions as $q(x)=q_{rot}(x)+q_{vib}(x)$; the hard-shell model is derived by setting $q(x)=q_{rot}(x)$. The convenient expressions adapted to Eq. (2) are given in the Appendix.

III. SYSTEMATICS OF THE SPECTRAL PROFILES

The inelasticity function $q(x)$ generally takes one minimum and one maximum, which lead to a spectral profile with double peaks—i.e., the nearly elastic peak and the deeply inelastic peak. We examine their dependences on the potential and on the energy.

A. Effect of the three-body potential

The potentials $V(r,x,R_{eq})$ by different values of the three-body strength δ are compared in Fig. 1 with a result of the self-consistent field (SCF) calculation [7] in the collinear ($x=1$) and isosceles triangular ($x=0$) configurations. It is seen that the potential is sensitive to δ at $x=0$, while insensitive at $x=1$. The SCF potential in the energy range of $E=10-100$ eV is well reproduced by the strength of $\delta=0.2$.

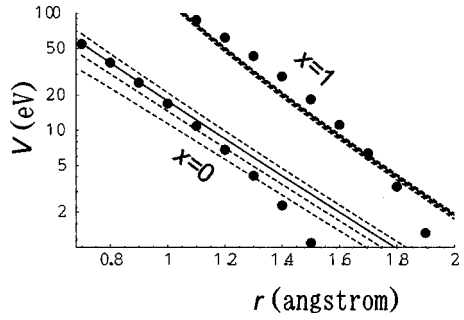

FIG. 1. Intermolecular potentials $V(r,x,R_{eq})$ for $Li^+ + N_2$ in the collinear ($x=1$) and isosceles triangular ($x=0$) configuration with the three-body strength of $\delta=0.2$ (solid lines) and with $\delta=0$, 0.1, and 0.3 (dashed lines). They are compared with the SCF calculation [7] (solid circles).

The equipotential surfaces at $E=16.8$ eV are plotted in Fig. 2. It is seen that the curvature at $x=0$ is sensitive to δ. A cave is formed by the pairwise potentials $V^{(2)}$ but filled in by the three-body correction $V^{(3)}$. In particular, the surface with $\delta=0.2$ gives a convex shape. The addition of $V^{(3)}$ is crucial to the spectra as demonstrated below.

Figure 3 shows the inelasticity functions at $E=16.8$ eV. It is seen that the rotational inelasticity $q_{rot}(x)$ takes a maximum at $x\sim\pm0.6$ and a vanishing minimum at $x=0$ and $x=\pm1$. The maximum value decreases as δ increases, reflecting a more isotropic shape of the surface. However, the total inelasticity $q(x)$ takes a maximum q_{max} at $x=\pm1$ and a minimum q_{min} at $x=0$, both contributed exclusively from vibrational excitation. In fact, they are expressed from Eq. (A7) as

$$q_{max}=\frac{m}{M}\left(\frac{\partial V/\partial R}{\partial V/\partial r}\right)^2_{r=r_\parallel,x=\pm1},\quad q_{min}=\frac{m}{M}\left(\frac{\partial V/\partial R}{\partial V/\partial r}\right)^2_{r=r_\perp,x=0},$$

with the major (minor) semiaxis $r_\parallel(r_\perp)$ of the surface. In these equations, the numerator in the parentheses represents a force upon vibration, while the denominator upon intermolecular repulsion. As observed in the figure, q_{max} is almost insensitive to δ because the two-body term $V^{(2)}$ dominates the potential in the collinear configuration. On the other hand, q_{min} rapidly decreases as δ increases, almost vanishing at $\delta=0.2$. This is because the force upon vibration rapidly

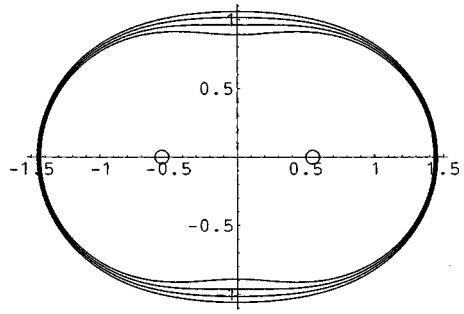

FIG. 2. Equipotential surfaces for $Li^+ + N_2$ at $E=16.8$ eV with the three-body strength of $\delta=0$, 0.1, 0.2, and 0.3. The surface expands as δ increases. The equilibrium nuclear positions in N_2 are shown by open circles. Scales are shown in Å.

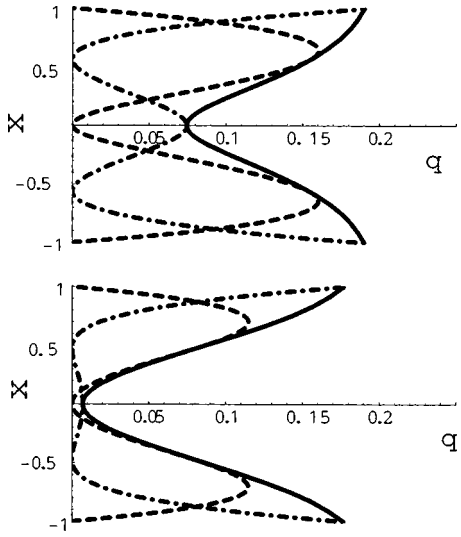

FIG. 3. Inelasticity functions for $^7Li^+ + N_2$ at $E=16.8$ eV using the three-body strength of $\delta=0$ (upper) and $\delta=0.2$ (lower). In respective panels are plotted $q(x)$ (solid curves), $q_{rot}(x)$ (dashed curves), and $q_{vib}(x)$ (dot-dashed curves).

decreases as $r_\perp$ increases and also because the force due to $V^{(3)}$ acts to shorten the N-N distance [see Eq. (1)] while $V^{(2)}$ to elongate.

Figure 4 shows the energy-loss spectra at $E=16.8$ eV with $\theta_{lab}=90°$ in the model and CT calculations, together with the experimental spectrum [6]. It is seen that, in the hard-shell model, the deeply inelastic peak moves towards smaller ϵ as δ increases, while the nearly elastic peak is located identically at $\epsilon=0$. In the hard-potential model, the deeply inelastic

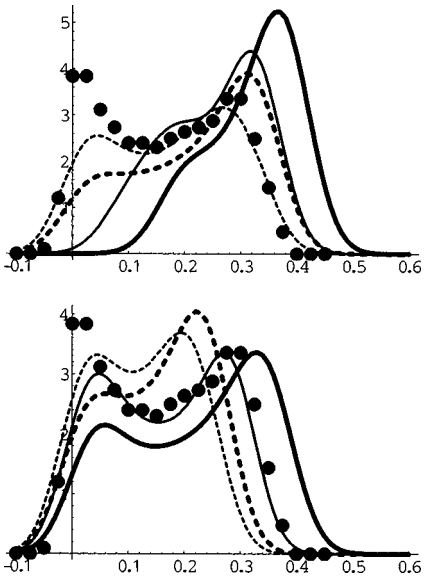

FIG. 4. Energy-loss spectra $f(\epsilon)$ in $^7Li^+ + N_2$ at $E=16.8$ eV with $\theta_{lab}=90°$ using the three-body strength of $\delta=0$ (upper) and $\delta=0.2$ (lower). Thick solid (dashed) curves indicate the hard-potential (hard-shell) model, while thin solid (dashed) curves show the vibrational-rotor (rigid-rotor) CT calculation. The FWHM of convolution is $\Delta\epsilon=0.10$. Solid circles indicate the experimental spectrum [6].

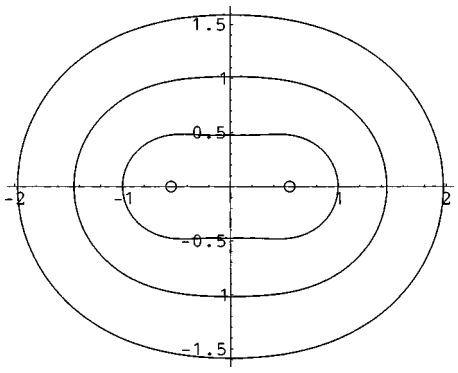

FIG. 5. Equipotential surfaces for $Li^+ + N_2$ at $E=2.1$, 16.8, and 134 eV. Open circles indicate the equilibrium nuclear positions in N_2. Scales are shown in Å.

peak is almost insensitive to δ, while the nearly elastic peak moves widely towards smaller ϵ as δ increases. These features are derived from the behaviors of $q_{rot}(x)$ and $q(x)$ described above. It is also seen that the spectra given by the vib-rotor (rigid-rotor) CT calculation almost follow those by the hard-potential (hard-shell) model, though giving noticeable shifts towards smaller ϵ for the deeply inelastic peak. This last point is related to the suddenness in a collision (see the following subsection). It is further noted that the experimental spectrum is well reproduced by the vibrational-rotor CT calculation with the potential of $\delta=0.2$ but not at all with $\delta=0$. This result confirms that the former potential is realistic and that the three- body correction is essential. We use the potential with $\delta=0.2$ through the analyses below.

B. Energy dependence

Figure 5 shows the equipotential surfaces at three energies in a geometrical progression. As the energy increases, the surface shrinks almost uniformly to give a more anisotropic shape, convex at $E=2.1$ eV and 16.8 eV but slightly concave around $x=0$ at $E=134$ eV. The inelasticity functions at the three energies are shown in Fig. 6 along with the lower panel in Fig. 3. Corresponding energy-loss spectra at $\theta_{lab}=90°$ by the model and CT calculations are shown in Fig. 7 along with the lower panel in Fig. 4.

In the models, the energy dependence of the spectra comes exclusively from that of $q(x)$ (see the Appendix). As seen from the figures, in the hard-shell model, the deeply inelastic peak moves towards larger ϵ as E increases. This behavior reflects the increase of the maximum in $q_{rot}(x)$, which is due to the increase of the anisotropy in the surface. In the hard-potential model, on the other hand, the nearly elastic peak moves towards larger ϵ as E increases. This behavior reflects the increase of the minimum in $q(x)$, which is related to the decrease of the surface curvature at $x=0$. It is noted in addition that, as E varies, the nearly elastic peak is almost unmoved (at $\epsilon\sim 0$) in the hard-shell model and so is the deeply inelastic peak (at $\epsilon\sim 0.35$) in the hard-potential model. Consequently, the model derives a shift due to vibrational excitation more conspicuously at lower energies for the deeply inelastic peak and at higher energies for the nearly elastic peak.

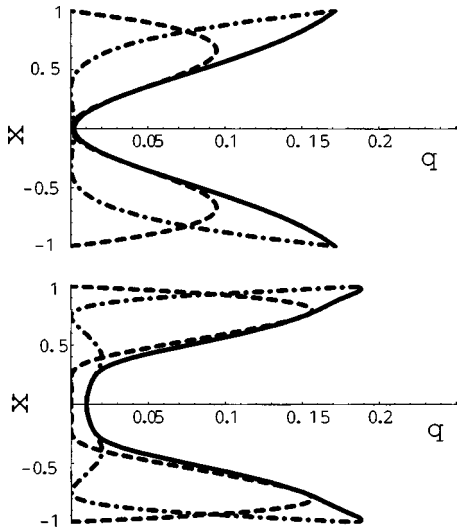

FIG. 6. Inelasticity functions for $^7Li^+ + N_2$ at $E=2.1$ eV (upper) and 134 eV (lower). In respective panels are plotted $q(x)$ (solid curves), $q_{rot}(x)$ (dashed curves), and $q_{vib}(x)$ (dot-dashed curves).

Through the spectra shown, the rigid-rotor CT calculation almost follows the hard-shell model though a small deviation is noticeable at higher energies. The vibrational-rotor CT calculation indicates a good agreement with the hard-potential model for the nearly elastic peak but a remarkable deviation for the deeply inelastic peak; the latter shows a good accordance at the highet energy (134 eV) but a wide shift at the lowest energy (2.1 eV). At $E=2.1$ eV, the vibrational-rotor CT calculation rather obeys the hard-shell model. These behaviors reflect the energy-dependent effect of vibrational excitation. This effect is also confirmed in the comparison between the rigid-rotor and vibrational-rotor CT calculations; they show a difference more significantly as E increases.

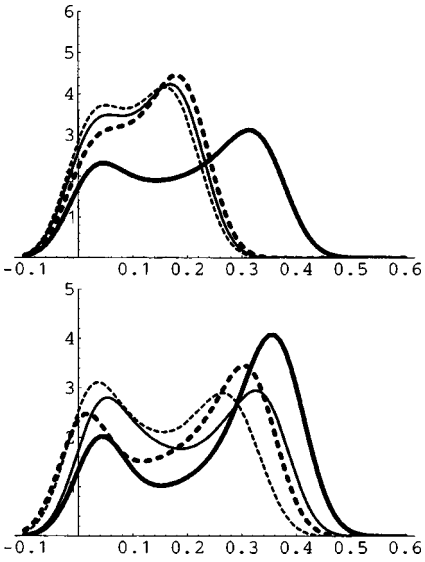

FIG. 7. Energy-loss spectra $f(\epsilon)$ in $^7Li^+ + N_2$ at $\theta_{lab}=90°$ with $E=2.1$ eV (upper) and 134 eV (lower). Thick solid (dashed) curves indicate the hard-potential (hard-shell) model, while thin solid (dashed) curves show the vibrational-rotor (rigid-rotor) CT calculation. The FWHM of convolution is $\Delta\epsilon=0.10$.

TABLE I. Rotational and vibrational suddenness parameters at different energies E.

E (eV)	$\omega_{rot}\tau_{col}$	$\omega_{vib}\tau_{col}$	Fig. No.
2.1	0.09	3.2	Fig. 7
8.4	0.10	1.6	Fig. 9
16.8	0.10	1.1	Figs. 4 and 8
57	0.10	0.60	Fig. 9
99	0.11	0.46	Fig. 9
134	0.14	0.40	Fig. 7

The findings above are understandable in terms of the suddenness in a collision. The rotational and vibrational suddenness parameters are introduced [4,18] and estimated in Table I using respective angular frequencies (ω_{rot} and ω_{vib}) together with a collision time τ_{col} given by a passing range 2λ. It is expected from the table that rotational excitation fully occurs through the energies because $\omega_{rot}\tau_{col} \ll 1$ (rotationally sudden), though getting less perfect as E increases. In addition, at the highest energy (134 eV), vibrational excitation also fully occurs because $\omega_{vib}\tau_{col} \ll 1$ (vibrationally sudden). This situation is near the sudden limit $\tau_{col} \to 0$ described by the hard-potential model. In reality, while the external impulsive force $V(r,x,R)$ causes a departure from the equilibrium length R_{eq}, the restoring force $U(R)$ acts as a brake on vibrational excitation during a finite collision time τ_{col}. Thus, vibrational excitation takes place less conspicuously as E decreases, reflecting worse vibrational suddenness. At the lowest energy (2.1 eV), vibrational excitation hardly occurs because $\omega_{vib}\tau_{col} \gg 1$ (vibrationally adiabatic). This situation is described by the hard-shell model.

We add a remark that the shift of the deeply inelastic peak between the hard-shell and hard-potential models is diminished as E increases (see Figs. 6 and 7). In consequence, even at $E=134$ eV, the shift between the rigid-rotor and vibrational-rotor CT calculations is as small as 10% of the maximum energy loss in spite of good vibrational suddenness.

IV. RESULTS AND DISCUSSION

A. Analysis of experimental spectra

Experimental energy-loss spectra [6–8] at different energies and angles are compared with the model and CT calculations in Figs. 8 and 9. It is seen that the spectra measured persistently indicate a profile with double peaks and that they are well reproduced by the vibrational-rotor CT calculation.

Figure 8 along with the lower panel of Fig. 4 shows the spectra in a wide range of angles ($\theta_{lab}=60°$, 90°, and 120°) at $E=16.8$ eV. It is seen that the angle dependence is virtually explained by the hard-potential model, where the spectra are derived from a common inelasticity function $q(x)$ (see the lower panel in Fig. 3). In particular, the deeply inelastic peak moves towards larger ϵ with the angle according to the kinematical relation of Eq. (A4), which gives the approximate scaling behavior with $1-\cos\theta_{lab}$. It is further noted that the

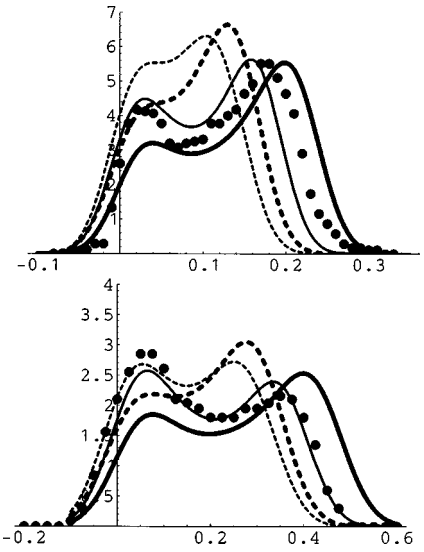

FIG. 8. Energy-loss spectra $f(\epsilon)$ in $^7Li^+ + N_2$ with $E=16.8$ eV at $\theta_{lab}=60°$ (upper) and 120° (lower). Thick solid (dashed) curves indicate the hard-potential (hard-shell) model, while thin solid (dashed) curves show the vibrational-rotor (rigid-rotor) CT calculation. The FWHM of convolution is $\Delta\epsilon=0.067$ for $\theta_{lab}=60°$ and $\Delta\epsilon=0.13$ for $\theta_{lab}=120°$. Solid circles indicate the experimental spectra [6].

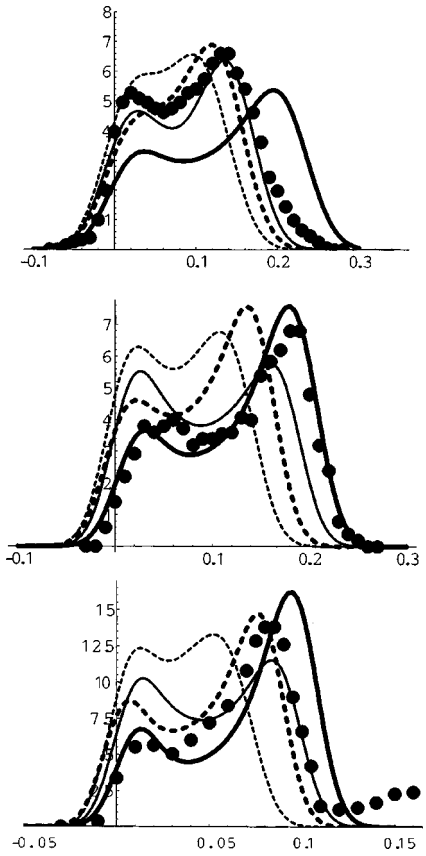

FIG. 9. Energy-loss spectra $f(\epsilon)$ for (a) $^7Li^+ + N_2$ at $\theta_{lab}=60°$ with $E=8.4$ eV (upper), (b) $^6Li^+ + N_2$ at $\theta_{lab}=60°$ with $E=57$ eV (middle), and (c) $^6Li^+ + N_2$ at $\theta_{lab}=40°$ with $E=99$ eV (lower). Thick solid (dashed) curves indicate the hard-potential (hard-shell) model, while thin solid (dashed) curves show the vibrational-rotor (rigid-rotor) CT calculation. The FWHM of convolution is $\Delta\epsilon=0.067$ for (a), 0.050 for (b), and 0.025 for (c). Solid circles indicate the experimental spectra [6] for (a), [8] for (b), and [7] for (c). Note that the experimental spectrum in (c) is accompanied in $\epsilon>0.12$ by an extra bump due to electronic excitation (see [7]).

relative heights of the double peaks vary with the angle. In the measurement [6] and in the vibrational-rotor calculation, the deeply inelastic peak is higher (lower) than the nearly elastic peak at 60° (at 120°). This trend is explained by the hard-potential model, though inperfectly, as coming from the Jacobian for solid angle elements between the center-of-mass and laboratory frames. In fact, Eq. (A3) indicates an increase (a decrease) of the Jacobian with increasing ϵ at 60° (at 120°).

Figure 9 shows the spectra in a wide range of energies ($E=8-100$ eV) at $\theta_{lab}=40°$ and 60°. The measurement at $E=8.4$ eV [6] indicates a spectral profile much more like the hard-shell model than like the hard-potential model. This comparison means that the spectrum is dominantly contributed from rotational excitation. It is explainable with the vibrational suddenness parameter as $\omega_{vib}\tau_{col}>1$ (see Table I). On the other hand, the spectra measured at $E=57$ eV [8] and 99 eV [7] evidently depart from the hard-shell model and behave rather like the hard-potential model. This means that vibrational excitation occurs conspicuously, explainable with $\omega_{vib}\tau_{col}<1$ (see Table I).

B. Analysis of a previous calculation

The soundest theoretical analysis for $Li^+ + N_2$ collisions so far has been made by Vilallonga and Micha [12]. They developed the time-correlation-function (TCF) method [11] using the Magnus expansion [19] for vibrational excitation and a sudden approximation for rotational excitation along with the classical trajectories for intermolecular motion. They took a potential calculated by Staemmler [20] and fitted by Billing [21] with the Legendre expansion. Applying these methods, Vilallonga and Micha [12] have analyzed the energy-loss spectra at $E=4-17$ eV and derived gross profiles with double peaks. However, they are not quite alike the measurements [6], in particular at larger angles. As a typical example, the spectrum at $\theta_{lab}=90°$ with $E=16.8$ eV is shown in the lower panel of Fig. 10, where the deeply inelastic peak calculated by them is widely shifted towards higher energy loss in comparison with the experiment. Such a deviation does not occur in the present analysis (see the corresponding spectrum shown in the lower panel of Fig. 4). It has been unclear whether this unacceptable result is due to the method of dynamical calculation or to the potential taken.

To get insight into this problem, we apply the hard-potential model with the same (Staemmler-Billing) potential that Vilallonga and Micha [12] took in the TCF calculation. As seen from the figure the model derives a spectrum similar to the TCF calculation, reproducing the deeply inelastic peak at $\epsilon=0.53$ and a slightly concave structure around $\epsilon=0.45$. These observations suggest that the potential taken was responsible.

To further illuminate this point, we plot the inelasticity functions by the Staemmler-Billing potential in the upper

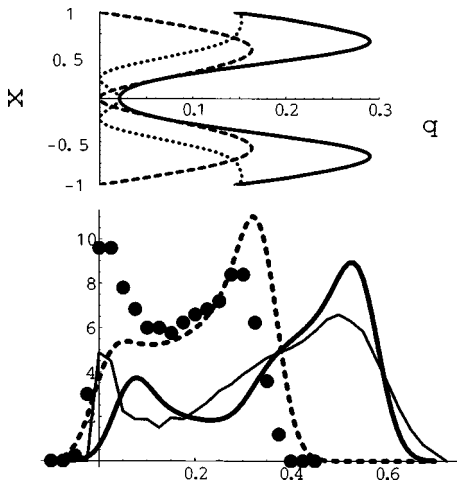

FIG. 10. Analysis with the Staemmler-Billing potential [21] for the energy-loss spectrum in $^7Li^+ + N_2$ at $\theta_{lab}=90°$ with $E=16.8$ eV. In the upper panel are plotted the inelasticity functions, $q(x)$ (solid curve), $q_{rot}(x)$ (dashed curve), and $q_{vib}(x)$ (dash-dotted curve). In the lower panel are plotted the results of the experiment [6] (solid circles), the time-correlation-function method [12] (a thin solid curve), the hard-potential model (a thick solid curve), and the hard-shell model (a thick dashed curve). The spectra in the models are convoluted with the FWHM of $\Delta\epsilon=0.083$.

panel of Fig. 10 and contrast them with the spectra shown in the lower panel. It is seen that the deeply inelastic peak comes from a maximum of $q(x)$ at $x \simeq \pm 0.7$ while the cancave structure arises from a contribution around $x=\pm 1$. The latter is accounted for by a "step" structure [22], which accompanies the deeply inelastic peak when $dq/d|x|<0$ at $x=\pm 1$. These features are obviously far from the present analysis, where $dq/d|x|>0$ near $|x|=1$ and the maximum appears at $x=\pm 1$ (see the lower panel in Fig. 3 for $E=16.8$ eV). While giving similar $q_{rot}(x)$, the two potentials derive completely different $q_{vib}(x)$; their potential leads to a rise as $|x|$ departs from 1, while ours to a steep fall. It is thus concluded that the unacceptable spectra obtained in the TCF calculation [12] are ascribable to the character of the Staemmler-Billing potential relevant to vibrational excitation. It is also remarked that this difficulty in the potential is not remedied by the procedure [12] of reducing the vibrational coupling strength because it does not alter the functional form of $q_{vib}(x)$.

The potential originally obtained by Staemmler [20] is almost consistent with ours used in the present analysis. However, his calculation was applied only to the equilibrium bond length R_{eq} except at the orientations of $x=0$ and $x=\pm 1$. Hence, we guess that the poor sampling points lead to the inaccurate fitting potential [21] for vibrational excitation.

V. CONCLUDING REMARKS

We have analyzed the energy-loss spectra in $Li^+ + N_2$ scatterings for a wide range of energies ($E=8-100$ eV) and angles ($\theta_{lab}=40°-120°$). The respective roles of rotational and vibrational excitations have been revealed through systematic comparisons of the experimental spectra with the model and CT calculations. The spectral profile and its energy dependence are related to the shape of the equipotential surface. The effect of vibrational excitation manifests itself in the shifts of double peaks. The nearly elastic peak is sensitive to the surface curvature at the orientation angle of 90°, hence to the three-body potential; the deeply inelastic peak reflects the vibrational suddenness in a collision. It is found that rotational excitation is dominant at lower energies (<10 eV), while vibrational excitation is remarkable at higher energies (~ 100 eV). The unacceptable result of a previous semiclassical calculation by Vilallonga and Micha is suggested to come from the inappropriate potential taken.

The combined application of the hard-shell and hard-potential models has been demonstrated to be useful for examining how rotational and vibrational excitations contribute to the spectra and how the spectral profile varies with energies, angles, and potentials. The analysis in this way will be promising for different diatomic molecules including heteronuclear ones.

ACKNOWLEDGMENTS

We are grateful to Professor S. Kita (Nagoya Institute of Technology) and Professor H. Tanuma (Tokyo Metropolitan University) for valuable discussion and for giving us the unpublished data. We thank to Professor K. Takayanagi and Professor Y. Itikawa (ISAS) for their suggestions in the early stage of this work. Acknowledgments are extended to Professor S. Yabushita (Keio University) for his comments on potential calculations. Numerical calculations have been done at the computer center of College of Science and Technology, Nihon University.

APPENDIX: ENERGY-LOSS SPECTRA IN THE HARD-POTENTIAL MODEL

The convoluted energy-loss spectrum [Eq. (2)] at the laboratory angle θ_{lab} is written as an integral over the equipotential surface,

$$\left\langle \frac{d\sigma}{d\epsilon d\Omega_{lab}} \right\rangle_{\Delta\epsilon} = \int_{-1}^{1} dx \frac{dS}{dx} F(q(x);\epsilon,\theta_{lab}), \tag{A1}$$

where the integrand is given by a composite function of $q(x)$ and

$$F(q;\epsilon,\theta_{lab}) = \frac{\partial(\Omega)}{\partial(\Omega_{lab})}\bigg|_{\epsilon^*} \frac{(1+q)^2[1-\epsilon^*(q)]I_{\Delta\epsilon}(\epsilon^*(q)-\epsilon)}{16\pi|(1+q)\sqrt{1-\epsilon^*(q)}-q\cos\theta^*(q)|}, \tag{A2}$$

with the Jacobian for solid-angle elements

$$\frac{\partial(\Omega)}{\partial(\Omega_{lab})}\bigg|_{\epsilon^*} = \left(\frac{\sin\theta^*(q)}{\sin\theta_{lab}}\right)^2 \frac{1}{\cos[\theta^*(q)-\theta_{lab}]}. \tag{A3}$$

In these equations, the scaled energy-loss and the center-of-mass angle are determined as

$$\epsilon^*(q) = \frac{2q}{(1+q)^2}[1 + \tilde{q}\sin^2\theta_{\rm lab} - \cos\theta_{\rm lab}\sqrt{1-\tilde{q}^2\sin^2\theta_{\rm lab}}], \tag{A4}$$

$$\cos\theta^*(q) = -\frac{\mu}{\sqrt{1-\epsilon^*(q)}}\sin^2\theta_{\rm lab} + \cos\theta_{\rm lab}\sqrt{1-\frac{\mu^2}{1-\epsilon^*(q)}\sin^2\theta_{\rm lab}}, \tag{A5}$$

where μ is the projectile-to-target mass ratio and $\tilde{q}=q+\mu+q\mu$. The surface element and the inelasticity function are given by a representation $r=r_S(x,R)$ of the surface as

$$\frac{dS}{dx} = 2\pi R_{\rm eq}^2 u(x)\sqrt{u^2(x)+(1-x^2)u'^2(x)}, \tag{A6}$$

$$q(x) = \frac{m}{M}u^2(x)\frac{v^2(x)+(1-x^2)u'^2(x)}{u^2(x)+(1-x^2)u'^2(x)}, \tag{A7}$$

where $u(x)=r_S/R_{\rm eq}$ and $v(x)=\partial r_S/\partial R$ at $R=R_{\rm eq}$, with m and M denoting the inter- and intramolecular reduced masses, respectively.

[1] D. Beck, U. Ross, and W. Schepper, Z. Phys. A **293**, 107 (1979); **299**, 97 (1981).

[2] W. Schepper, U. Ross, and D. Beck, Z. Phys. A **290**,131 (1979); D. Beck, Chem. Phys. **126**, 19 (1988); M. Velegrakis and D. Beck, J. Chem. Phys. **94**, 7981 (1991); D. Beck, in *Physics of Electronic and Atomic Collisions* edited by S. Datz (North-Holland, Amsterdam, 1982), p. 331.

[3] T. Hasegawa, S. Kita, and H. Inouye, J. Phys. B **18**, 3775 (1985); M. Nakamura, S. Kita, and T. Hasegawa, J. Phys. Soc. Jpn. **56**, 3161 (1987).

[4] A. Ichimura and M. Nakamura, Phys. Rev. A **69**, 022716 (2004).

[5] R. Boettner, U. Ross, and J. P. Toennies, J. Chem. Phys. **65**, 733 (1976).

[6] U. Gierz, J. P. Toennies, and M. Wilde, Chem. Phys. Lett. **110**, 115 (1984).

[7] S. Kita, H. Tanuma, I. Kusunoki, Y. Sato, and N. Shimakura, Phys. Rev. A **42**, 367 (1990).

[8] S. Kita and H. Tanuma (unpublished).

[9] G. A. Pfeffer and D. Secrest, J. Chem. Phys. **78**, 3052 (1983).

[10] R. D. Sharma, P. M. Bakshi, and J. M. Sindoni, Phys. Rev. A **43**, 189 (1991); H. Dothe and R. D. Sharma, J. Chem. Phys. **98**, 4567 (1993).

[11] E. Vilallonga and D. A. Micha, J. Chem. Phys. **84**, 3162 (1986); **86**, 750 (1987).

[12] E. Vilallonga and D. A. Micha, J. Chem. Phys. **86**, 760 (1987).

[13] S. Ikuta, Chem. Phys. **95**, 235 (1985).

[14] S. T. Grice, P. W. Harlamd, and R. G. A. R. Maclagan, Chem. Phys. **165**, 73 (1992).

[15] M. F. Falcetta and P. E. Siska, J. Chem. Phys. **109**, 6615 (1998).

[16] T. Ishikawa, S. Kita, and H. Inouye, Bull. Res. Inst. Sci. Meas. Tohoku Univ. **24**, 101 (1976).

[17] H. Tanuma, S. Kita, I. Kusunoki, and N. Shimakura, Phys. Rev. A **38**, 5053 (1988).

[18] M. Nakamura, J. Phys. Soc. Jpn. **56**, 3145 (1987).

[19] W. Magnus, Commun. Pure Appl. Math. **7**, 649 (1954).

[20] V. Staemmler, Chem. Phys. **7**, 17 (1975).

[21] G. D. Billing, Chem. Phys. **36**, 127 (1979).

[22] For the definition of the "step" in the hard-potential model, see Eq. (29) in Ref. [4].